ELSEVIER

Contents lists available at ScienceDirect

Agricultural and Forest Meteorology

journal homepage: www.elsevier.com/locate/agrformet



Proximal remote sensing and gross primary productivity in a temperate salt marsh

Alma Vázquez-Lule¹, Rodrigo Vargas^{*}

Department of Plant and Soil Sciences, University of Delaware, Newark, DE, USA

ARTICLE INFO

Keywords: Canopy phenology Hyperspectral Modeling Wetland Photosynthesis Solar induced fluorescence

ABSTRACT

Salt marshes are highly productive ecosystems relevant for Blue Carbon assessments, but information for estimating gross primary productivity (GPP) from proximal remote sensing (PRS) is limited. Temperate salt marshes have seasonal canopy structure and metabolism changes, defining different canopy phenological phases, GPP rates, and spectral reflectance. We combined multi-annual PRS data (i.e., PhenoCam, discrete hyperspectral measurements, and automated spectral reflectance sensors) with GPP derived from eddy covariance. We tested the performance of empirical models to predict GPP from 12 common vegetation indices (VIs; e.g., NDVI, EVI, PSRI, GCC), Sun-Induced Fluorescence (SIF), and reflectance from different areas of the electromagnetic spectrum (i.e., VIS-IR, RedEdge, IR, and SIF) across the annual cycle and canopy phenological phases (i.e., Greenup, Maturity, Senescence, and Dormancy). Plant Senescence Reflectance Index (PSRI) from hyperspectral data and the Greenness Index (GCC) from PhenoCam, showed the strongest relationship with daily GPP across the annual cycle and within phenological phases (r^2 =0.30-0.92). Information from the visible-infrared electromagnetic region (VIS-IR) coupled with a partial least square approach (PLSR) showed the highest data-model agreement with GPP, mainly because of its relevance to respond to physiological and structural changes in the canopy, compared with indices (e.g., GCC) that particularly react to changes in the greenness of the canopy. The most relevant electromagnetic regions to model GPP were ~550 nm and ~710 nm. Canopy phenological phases impose challenges for modeling GPP with VIs and the PLSR approach, particularly during Maturity, Senescence, and Dormancy. As more eddy covariance sites are established in salt marshes, the application of PRS can be widely tested. Our results highlight the potential to use canopy reflectance from the visible spectrum region for modeling annual GPP in salt marshes as an example of advances within the AmeriFlux network,

1. Introduction

Salt marshes are highly productive ecosystems relevant to the local-to-global carbon cycle (Hayes et al., 2018) but need better representation of their function as part of the coastal interface in Earth System Models (Ward et al., 2020). Gross primary productivity (GPP) is a critical element of the carbon stored in salt marshes, and consequently, accurate estimations are essential for closing the carbon budget (Alongi, 2020; Eagin et al., 2020). This flux is primarily regulated by plant phenology associated with changes in light, temperature, nutrient availability, and hydrological patterns (Knox et al., 2017; Lu et al., 2017; Vázquez-Lule et al., 2022). In recent years, ecosystem-scale GPP has been estimated using the eddy covariance (EC) technique in wetlands (Forbrich et al., 2018; Knox et al., 2017; Lu et al., 2017), and this

information has been coupled with spaceborne data to estimate GPP at the regional scale (Eagin et al., 2020). Furthermore, spectral properties of canopy reflectance have proven helpful in representing the temporal variability of GPP in salt marshes (Eagin et al., 2020; Hill et al., 2021; Tao et al., 2018; Vázquez-Lule et al., 2022). That said, there is a need to improve the application of spectral reflectance derived from different platforms to better represent GPP from salt marshes in regional and global models (Ryu et al., 2019; Ward et al., 2020).

Applying remote sensing tools in coastal areas is challenging because atmospheric scattering effects can impact the reflectance data collected by airborne and satellite spectrometers (Malthus and Mumby, 2003). Coastal regions with higher levels of atmospheric vapor are particularly prone to this issue, as it can impact how the near-infrared region interacts with the land surface reflectance (Adam et al., 2010). As an

^{*} Corresponding author.

E-mail address: rvargas@udel.edu (R. Vargas).

Climate Change, Energy and Low Carbon Development, Center for International Forestry Research (CIFOR), Bogor, Indonesia.

alternative, Proximal Remote Sensing (PRS; e.g., handheld spectrometers, spectral sensors, and phenological cameras [PhenoCam]) is a feasible and cost-effective tool to monitor and predict GPP and salt marsh ecosystem productivity (Hill et al., 2021; Knox et al., 2017), and it is appealing for ecological studies, as it also reduces the atmospheric influence on the collection of canopy irradiance and reflectance, and allows for finer scale observations and analysis (Matthes et al., 2015; Richardson, 2019; Vázquez-Lule et al., 2022). In addition, PRS is a relevant component for increasing the footprint of ground-truth information required for upscaling reflectance from the ecosystems to the landscape scale (Asner and Martin, 2016; Porcar-Castell et al., 2014). However, there are substantial differences in the available PRS tools; some of them are related to the spatial region of interest covered, the temporal resolution of data collected, and the spectral composition of data and derived products (Richardson, 2019; Rossini et al., 2010; Hill et al., 2021). Those properties may have a different sensitivity to model GPP in coastal wetlands; therefore, intensive research is needed.

Recently, the capabilities of PRS to monitor and predict GPP have increased through the collection and usability of multi and hyperspectral data (Dechant et al., 2020; Inoue et al., 2008; Kim et al., 2021; Rossini et al., 2010). Hyperspectral data from PRS can be used to derive vegetation indices (VIs), the Sun-Induced Fluorescence (SIF), and in multivariate approaches to provide insights about the temporal variability of GPP and other plant traits (Dechant et al., 2020; Inoue et al., 2008; Rossini et al., 2010; Zarco-Tejada et al., 2013). Generally, methods to model GPP from spectral data are grouped into parametric and non-parametric. Parametric approaches are used to derive well-known spectral VIs - such as Normalized Difference Vegetation Index (NDVI), Enhanced Vegetation Index (EVI), or Photochemical Reflectance Index (PRI) - that can relate to GPP (Inoue et al., 2008; Rossini et al., 2010; Zarco-Tejada et al., 2013). Non-parametric approaches, such as the Partial Least Square Regression (PLSR), have also been used for data-model agreement of GPP with hyperspectral data (Cheng et al., 2020; Dechant et al., 2019; DuBois et al., 2018; Matthes et al., 2015). PLSR is based on optimizing models by their learning and training with the properties under study (i.e., GPP). It can reduce the spectral information to a set of latent variables and improve relationships between the hyperspectral reflectance and GPP by capturing data from many individual regressions at once (Matthes et al., 2015; Serbin et al., 2016). In addition, the use of PLSR with hyperspectral data to model GPP gives the availability to test the individual or collective performance of electromagnetic regions that may explain different properties in vegetation, such as the Infrared region (IR) that is related to changes in the physiological condition of vegetation or the red edge region (RedEdge) that shows the most contrasting differences between the absorption of red light during the photosynthesis and the physiological state of vegetation.

More recently, information derived from SIF has been used as a proxy for GPP across terrestrial ecosystems (Kim et al., 2021; Miao et al., 2018; Yang et al., 2018; Zarco-Tejada et al., 2013). SIF is a dissipated way of energy during the light reactions of photosynthesis, as it is the radiative loss of energy that absorbs and remits photons (Meroni et al., 2009; Porcar-Castell et al., 2014). SIF can be estimated from irradiances collected by hyperspectral PRS using the Fraunhofer lines depth/discriminator (FLD) method. The FDL is one of the most suitable methods to passively assess SIF on the dark parts of the electromagnetic region as a response to the absorption of gases from the atmosphere (e.g., O2). Then radiances emitted on some of those lines correspond to SIF emissions from the vegetation activity (Porcar-Castell et al., 2014). SIF estimations are sensitive to changes in the Ecosystem-Scale GPP from the daily and annual variability across different terrestrial ecosystems (Rossini et al., 2010; Zarco-Tejada et al., 2013); however, information is lacking for testing the applicability of SIF to estimate GPP across canopy phenological phases in salt marshes.

The AmeriFlux network has exponentially grown in the last 25 years, but several ecosystems still need to be better represented across the

United States (Villarreal et al., 2018) and Latin America (Villarreal and Vargas, 2021). Interest in carbon dynamics in salt marshes has increased in the previous decade, but their representation within AmeriFlux and FLUXENT still lags behind freshwater wetlands and terrestrial ecosystems (Delwiche et al., 2021). The main goal of this study was to identify the spectral properties of reflectance data from PRS that could be useful to model and predict daily GPP in a salt marsh across the annual cycle and during different canopy phenological phases. For this purpose, we tested different VIs, SIF, and areas of the electromagnetic spectrum between 480 and 820 nm. We coupled information from automatic and manual canopy spectral reflectance from PRS instruments with GPP during three years of study (2016 to 2018).

We asked three interrelated questions: (1) How does hyperspectral reflectance characterize the salt marsh GPP across different canopy phenological phases (i.e., Greenup, Maturity, Senescence, and Dormancy)?; (2) What are the individual performance of different VIs and SIF estimations to model daily GPP?; (3) How do different electromagnetic regions (i.e., Visible and Infrared (VIS-IR); red edge (RedEdge); Infrared (IR) and SIF) from hyperspectral PRS perform to model daily GPP? We hypothesized that hyperspectral reflectance would show different patterns and magnitudes across the electromagnetic regions for each canopy phenological phase as a response to changes in growth and greenness patterns (Zhu et al., 2010). We expected that SIF would show a strong relationship with daily GPP compared with any other relationship between GPP and VIs as a result of the documented association of SIF with photosynthesis in other ecosystems (Dechant et al., 2020; Li et al., 2018; Zarco-Tejada et al., 2013; Zhang et al., 2018). In addition, we hypothesized that the RedEdge region would show a robust data-model agreement with GPP compared with other electromagnetic regions, mainly because it shows a higher reflectance contrast between the region that relates with the absorption of light by chlorophyll pigments (i.e., red) and the IR region that associates with the physiological condition of vegetation (Cheng et al., 2020; Dechant et al., 2019; Matthes et al., 2015).

2. Materials and methods

2.1. Study site

The study site is a temperate tidal salt marsh dominated by grasses at the St. Jones Reserve, Delaware, USA (39°05′ 17.49″, 75°26′14.00″). The dominant plant species is Spartina alterniflora (~66% of the area) (=Sporobolus alterniflorus (Loisel.); Peterson et al. 2014), followed by Spartina cynosuroides (i.e., ~29% of the area) (=Sporobolus cynosuroides (L.); Peterson et al. 2014) and Phragmites australis (i.e., <5% of the area). This ecosystem has four distinct canopy phenological phases across the annual cycle: Greenup, when grasses start to grow, and their greenness and GPP have a linear increase, usually in the study site from April to June, in addition during this phase, the GPP increases, making of this ecosystem a net sink of carbon; Maturity, when grasses reach their peak of growth and greenness, usually from July to September, also during this phase GPP is higher than ecosystem respiration and the salt marsh is a sink of carbon; Senescence, when grasses begin to decrease in greenness, and as well their defoliation starts, usually from September to October; during this phase as well as dormancy, respiration is larger than GPP and the ecosystem is a source of carbon to the atmosphere; and Dormancy, when grasses are inactive, and the GPP reach their lower point, this phenological phase is from November to March (Trifunovic et al., 2020; Vázquez-Lule and Vargas, 2021). At this study site, the soils are silty clay loam (Capooci et al., 2019), and tides are semidiurnal, with two similar high tides and low tides in 24 h (CEC, 2015). Tides at our site $\,$ rarely submerge the vegetation (only during extreme surge events) and consequently have little effect on influencing canopy spectral reflectance measurements (Hill et al., 2021; Vázquez-Lule et al., 2022).

The St. Jones Reserve is part of the Delaware National Estuarine Research Reserve and one of the National Estuarine Reserve Research System (NERRS) from the National Oceanic and Atmospheric Administration (NOAA, 2020). It is also part of the AmeriFlux Network (US-StJ), PhenoCam Network (stjones; Seyednasrollah et al. 2019), and SpecNet (US-Stj) (Fig. 1).

2.2. Eddy covariance measurements

We used three years of eddy covariance (EC) data to derive GPP from net ecosystem exchange (NEE) measurements (i.e., January 2016 to December 2018). The EC tower has a height of 3.5 m and was established in 2015. It has a WindMaster Pro anemometer, model 160724 (Gill Instruments, Lymington, Hampshire UK), and an LI-7200RS enclosed path CO2/H2O analyzer (LICOR Environmental, Lincoln, NE). The average footprint area of EC has a ratio of about 150 m around the tower, where 95% of fluxes are from dominant salt marsh species (i. e., S. alterniflora and S. cynosuroides; Fig. 1). We processed these data following standardized protocols for QA/QC, calculation of half-hour fluxes, and gap filling of NEE (Vázquez-Lule and Vargas, 2021). We applied a coordinate double-rotation for misalignments of the anemometer, a block average Reynolds decomposition for correction of fluctuations in turbulence, and the Webb-Pearman-Leuning correction for air density fluctuations when readings of the LI-7200RS thermopars were missing. For a more detailed description, see Vázquez-Lule and Vargas (2021). Half-hour estimates of GPP were calculated from partitioning NEE following standardized protocols based on the relationship of nighttime NEE with temperature (Reichstein et al., 2005); daily GPP was subsequently calculated from this time series. We used this data to estimate daily cumulative GPP. We tested for statistically significant differences in daily GPP across canopy phenological phases by comparing least square means and then using the Tukey post hoc test. For all the statistical analyses, GPP was used in original units after removing values higher than the GPP mean plus two standard deviation values (i.e., mean = 4.3 and SD = 4.7).

2.3. Proximal remote sensing instrumentation

We used an array of PRS instruments to collect automatic VIs from spectral reflectance sensors (i.e., Normalized Difference Vegetation Index $[NDVI_{(t)}]$ and the Photochemical Reflectance Index $[PRI_{(t)}]$, phenology camera's color band data (i.e., PhenoCam) and manually hyperspectral PRS data during the study period. These proximal sensors have different data collection frequencies; however, we standardize them as a daily collection (i.e., daily time steps). All PRS measurements were inside the EC tower's footprint area and represented the reflectance of the dominant salt marsh species in the ecosystem (i.e., *S. alterniflora* and *S. cynosuroides*).

2.3.1. Automatic measurements from spectral reflectance sensors

The Normalized Difference Vegetation Index (i.e., NDVI $_{(t)}$) and the Photochemical Reflectance Index (i.e., PRI $_{(t)}$) from automatic spectral reflectance sensors were used (Meter Inc, Pullman, WA, USA). These sensors were installed with a field view angle of ~45°, and their average footprint was around 1.5 m; they collected data every 5 min in two areas of the salt marsh (Hill et al., 2021; Vázquez-Lule et al., 2022; Fig. 1). We calculated daily averages of both vegetation indices considering measurements collected between 11:00 and 13:00 h local time to reduce the effect of variability at the light conditions following standardized protocols (Gamon et al., 2015; Hill et al., 2021).

2.3.2. PhenoCam

We used PhenoCam data collected every 30 min during the day (StarDot NetCam SC; StarDot Technologies, California, USA). A PhenoCam was installed in the upper part of the EC tower, and it collected continuous photographs in Red-Green-Blue and InfraRed. Salt marsh vegetation represented $\sim\!80\%$ of the camera's field range, and the data used for this analysis was inside the EC footprint area (Fig. 1). From PhenoCam data, we used data collected between 11:00 and 13:00 h local time to reduce the effect of variability in the light conditions (Hill et al.,

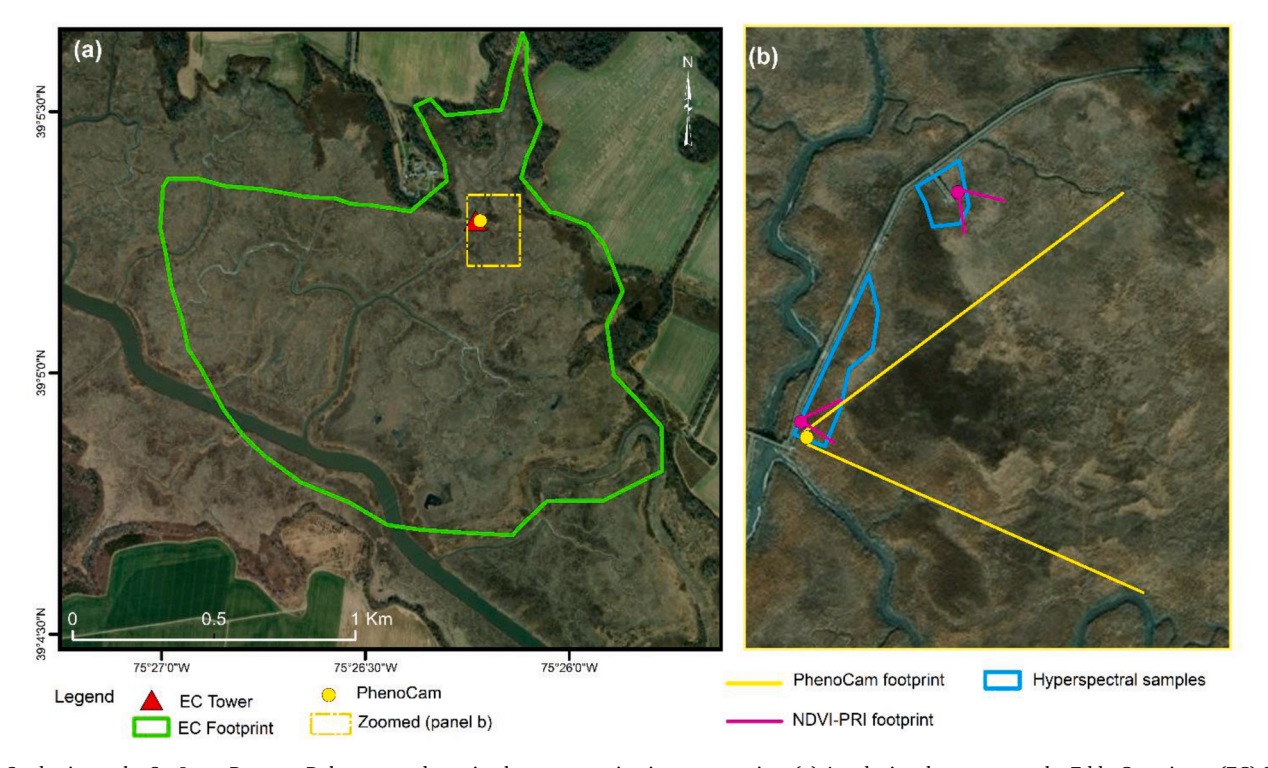


Fig. 1. Study site at the St. Jones Reserve, Delaware, and proximal remote sensing instrumentation. (a) A red triangle represents the Eddy Covariance (EC) System; the green light polygon represents the EC footprint; the yellow circle represents the location of the PhenoCam. (b) Closeup panel showing the proximal remote sensing instrumentation. Yellow lines represent the PhenoCam footprint; the NDVI-PRI footprint sensors are presented in magenta in two separate areas of the salt marsh, and the blue polygons highlight areas where the hyperspectral samples were collected.

2021). This data was used to calculate the daily Greenness Index (i.e., GCC) as the ratio of green digital numbers and the total digital numbers of all color bands (Red + Green + Blue). We used the Phenopix R package (Filippa et al., 2016) and the function "autofilter" and spline filter to estimate daily GCC (Migliavacca et al., 2011). The "green-Explore" function was used to fit phenology GCC curves for every year, and the "gu" method (Gu et al., 2009) to define the transition between canopy phenological phases based on a combination of local maximum GCC and the first derivative (Filippa et al., 2016; Gu et al., 2009; Trifunovic et al., 2020; Vázquez-Lule and Vargas 2021).

2.3.3. Hyperspectral sensors

We manually collected hyperspectral data with handheld spectrometers in an area of \sim 450 m² of vegetation inside the EC footprint. We measured the reflectance from the dominant salt marsh species and then averaged these samples to represent the reflectance at the canopy scale (Vázquez-Lule et al., 2022; Fig. 1). Two synchronized fiber optic spectrometers were used, one with a detector range of 480 to 820 nm and a spectral resolution of ~ 1 nm (S₄₈₀₋₈₂₀), and the other with a detector range of 720 to 800 nm with a spectral resolution ~ 0.08 nm (S_{720_800}) (Jaz Spectrometer, Ocean Optics, Dunedin, FL). Canopy surface relative irradiance was measured from stands of salt marsh vegetation about every 1.5 weeks from September 2016 to December 2018. All measurements were performed under stable light conditions between 8:00 am and 10:30 am during sunny days without clouds and partially cloudy conditions, at the height of \sim 2 m above the soil surface as described previously (Vázquez-Lule et al., 2022). The hyperspectral data collected was used to calculate VIs and SIF (see Section 2.4) and to model GPP with the PLSR approach (see Section 2.5).

For every measurement, we used a cosine corrector to filter the irradiance and all the samples were collected with a field view of 180° and with a perpendicular angle between the canopy and cosine (Vázquez-Lule et al., 2022). We also adjusted the integration time of the incoming light, then performed a dark calibration covering the cosine corrector with a black plastic cap, then registered the upwelling irradiance and, finally, the downwelling irradiance. Upwelling irradiance was registered every 2–3 samplings of downwelling irradiance, and dark calibration was performed after 10–20 samples of downwelling irradiance or as needed if light conditions changed. During every measurement campaign, we collected ~120 downwelling irradiance samples. We calculated the reflectance for every downwelling irradiance measurement as follows:

$$R = \frac{(S * W) - (D * W)}{(I * W) - (D * W)} \tag{1}$$

where, R is the calculated reflectance; S downwelling irradiance; W wavelength; D dark calibration value; and I upwelling irradiance. After reflectance was calculated for every downwelling sampling, we calculated the mean daily reflectance and its standard deviation (Vázquez-Lule et al., 2022). We showed the reflectance pattern by canopy phenological phases from the reflectance collected from both spectrometers (i.e., $S_{480-820}$ and $S_{720-800}$).

2.4. Vegetation indices and SIF estimation

We calculated common VIs, which have been correlated with GPP for grasses and rice paddies (Cerasoli et al., 2018; Inoue et al., 2008; Rossini et al., 2010; Zarco-Tejada et al., 2013; Zhang and Zhou, 2017) and are described in Table 1. The time series for these indices are shown in SM Fig. S1a–S1c. For this purpose, reflectance from the VIS-IR electromagnetic region at 1 nm of spectral resolution (i.e., $S_{480-820}$) was used. We performed linear regression models to test the relationship between GPP and each VIs across the annual cycle and by canopy phenological phases. In addition, we identified the contribution of VIs to model annual GPP with stepwise linear regression models (see supplementary

Table 1Spectral Vegetation Indices (VIs) used in this study for linear regression models with GPP across different canopy phenological phases.

Acronym VI	Name VI	Equation	Ref.		
CI	Chlorophyll Index	[R750-R705]/ [R750+R705]	(Gitelson and Merzlyak, 1994)		
CI-Green	Chlorophyl Index of Green	[R750/R550]-1	(Gitelson et al., 2005)		
CI- RedEdge	Chlorophyl Index of Red Edge	[R750/R710]-1	(Gitelson et al. 2005)		
EVI	Enhanced Vegetation Index	2.5*[R800-R670]/ [R800+6*R670- 7.5*R400+1]	(Huete et al., 2002)		
MCARI	Modified Chlorophyll Absorption Ratio Index	[(R750-R7100- 0.2*9R750-R550)]* [R750/R710)	(Wu et al., 2009)		
PSRI	Plant Senescence Reflectance Index	[R680-R500]/R750	(Merzlyak et al., 1999)		
RedEdge- NDVI-a	Red Edge NDVI	[R750-R710]/ [R750+R710]	(Gitelson and Merzlyak, 1996)		
RedEdge- NDVI-b	Red Edge NDVI	[R750-R720]/ [R750+R720]	(Gitelson and Merzlyak, 1994)		
sPRI	Modified Photochemical Reflectance Index	[(R531-R570)/ (R531+R570)+1]/2	(Gamon et al., 1992)		

materials).

SIF was calculated with a radiance-based approach, using the detector with a range of 720 to 800 nm and a spectral resolution of ~ 0.08 nm (S720–800). We applied the FLD method based on the difference between two flux measurements inside and outside the Fraunhofer Line. Fraunhofer Lines represent areas of the electromagnetic region with higher absorption of O2, meaning that the emitted energy on those lines represents the amount of SIF from the vegetation activity. To calculate SIF, we used a standard mathematical description of the FLD (Meroni et al., 2009), and the ~ 773.5 nm Fraunhofer Line (FL) as the highest point of SIF emission.

2.5. Data-model agreement between GPP and reflectance from different electromagnetic regions

Hyperspectral measurements were coupled with a PLSR approach to derive potential predictive models of GPP at this study site. The PLSR is a multivariate modeling method to identify the relationship and structure between two data matrices. It has the advantage of handling high collinearity in the predictor matrix due to more predictor variables than the observed matrix (Wold et al., 2001). We developed daily GPP models for the following scenarios of vegetation: (a) Annual cycle, including all canopy phenological phases (Annual $_{\rm WD}$); (b) Annual cycle without Dormancy phase (Annual $_{\rm nD}$); we included this scenario under the assumption that during Dormancy GPP in this ecosystem is neglectable; (c) Greenup; (d) Maturity; (e) Senescence; and (f) Dormancy.

We tested every scenario of canopy phenological phases with reflectance from four electromagnetic regions: (a) Visible and Infrared (VIS-IR, 480 to 820 nm; 1 nm spectral resolution); (b) Infrared (IR, 756 to 820 nm; 1 nm spectral resolution); (c) Red Edge (RedEdge 675 to 755 nm; 1 nm spectral resolution); and (d) SIF (760 to 786 nm; 0.08 nm spectral resolution). We followed the PLSR implementation provided by Serbin et al. (2016) and tested different PLSR models for every scenario. For every model, 70% of the data was used for model calibration and 30% for independent model validation. We used the PRESS (Prediction Residual Sum of Squares) metric as information criteria to assess the optimal number of components in the PLSR and to reduce the model overfitting (Vázquez-Lule et al., 2022). Consequently, for scenarios of the annual cycle (i.e., Annual_{wD}; Annual_{nD}), \leq 15 components were

used, and for all other scenarios (i.e., Greenup, Maturity, Senescence, and Dormancy), ≤ 8 components. We used a Jackknife resampling method with 1000 permutations and iterative cross-validation to test the stability and generality of models (Serbin et al., 2016).

For scenarios of the annual cycle, a 10-fold cross-validation was used, and for all other scenarios, a 2-fold cross-validation was used. The $\rm r^2$ coefficient, the root mean square error (RMSE), and the bias metric were used to evaluate the performance and uncertainty of every model (Serbin et al., 2016). Finally, an independent model validation with the remaining 30% of available data was performed. Results with over >30% of explained variance are reported to highlight the main findings of this study.

We computed the correlation of each nanometer on the different electromagnetic regions with GPP. Correlation coefficients are reported in a comparative graph for every scenario. We also estimated the variable importance in projection (VIP), which shows each nanometer's contribution to the overall prediction variance of GPP for each PLSR model (Meacham-Hensold et al., 2020; Serbin et al., 2016). VIP results are shown in comparative graphs for every electromagnetic region.

3. Results

3.1. Gross primary productivity and general climatology

During the study period, the annual mean GCC index was $0.34\pm0.03,$ with lower values during Dormancy (0.31 ± 0.01) and higher values during Maturity $(0.38\pm0.01;$ Fig. 2a). PAR had an annual mean of $139\pm77~\mu mol~m^{-2}~s^{-1},$ with lower values during Dormancy $(97\pm57~\mu mol~m^{-2}~s^{-1})$

 $m^{-2}~s^{-1})$ and higher values during Maturity (212±58 µmol $m^{-2}~s^{-1};$ Fig. 2b). The annual mean air temperature was 14±9 °C with lower temperature during Dormancy (6±6 °C) and higher temperature during Maturity (25±3 °C; Fig. 2c). Salinity had an annual mean of 5±4 ppm, with lower values during Dormancy (3.5±3 ppm) and higher values during Maturity (10±4 ppm, Fig. 2d). The daily annual cumulative mean of GPP was 4.2±4.2 g C-CO₂ m^{-2} , with lower values during Dormancy (0.68±0.55 g C-CO₂ m^{-2}) and higher values during Maturity (9.8±2.9 g C-CO₂ m^{-2} ; Figs. 2e and 3). Daily GPP was significantly different between all canopy phenological phases (p <0.05; Fig. 3)

3.2. Reflectance across canopy phenological phases

We found that Greenup, Maturity, and Senescence showed a similar reflectance pattern across the VIS-IR electromagnetic region, with differing magnitudes of reflectance. The main differences between that reflectance were $\sim\!550$ nm, $\sim\!700$ nm, and the slope from $\sim\!700$ to 740 nm (Fig. 4a–c). Dormancy showed an almost linear reflectance increase from 480 to 820 nm (Fig. 4d). During Senescence, two reflectance samples showed a similar response to reflectance samples during Maturity, and those samples were excluded from future analyses (Fig. 4c). Although those measurements fall within Senescence, dates were relatively close to the Maturity phase, and the reflectance magnitudes were more like Maturity than Senescence.

We found similar reflectance patterns for the SIF electromagnetic region (760 to 786 nm, 0.08 nm spectral resolution) for Greenup, Maturity, and Senescence, with substantial differences between 770 and 775 nm, mainly on the FL used to calculate SIF (773.5 nm; Fig. 4e–g). In

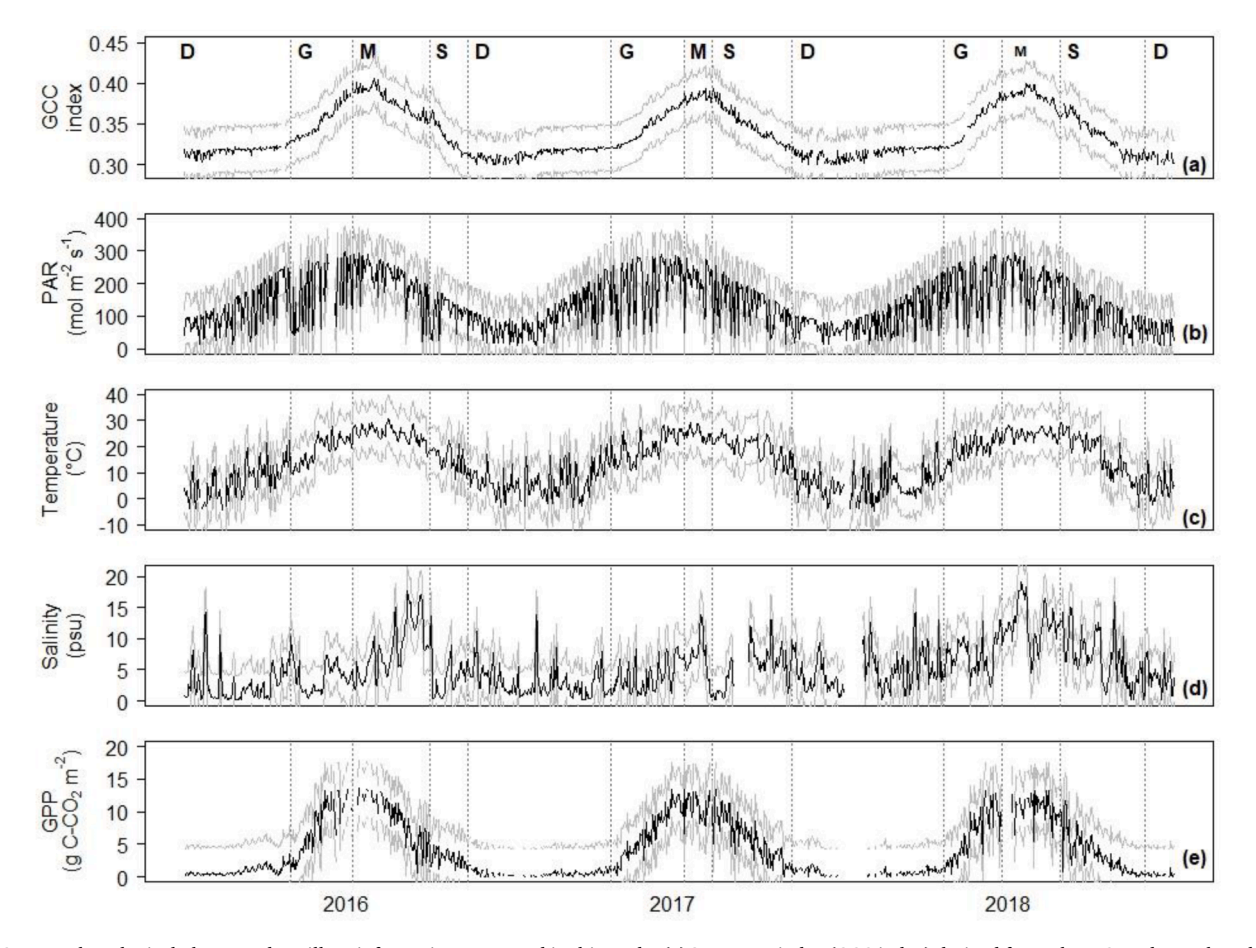


Fig. 2. Canopy phenological phases and ancillary information were used in this study. (a) Greenness index (GCC index) derived from PhenoCam data, where letters at the top represent canopy phenological phases: D, Dormancy; G, Greenup; M, Maturity; S, Senescence. (b) Daily photosynthetic active radiation (PAR), (c) Air temperature (Temperature), (d) Salinity, and (e) Daily sum of gross primary productivity (GPP) in the study site. Mean daily values are in black and mean (or sum for GPP) \pm one standard deviation values are in light gray.

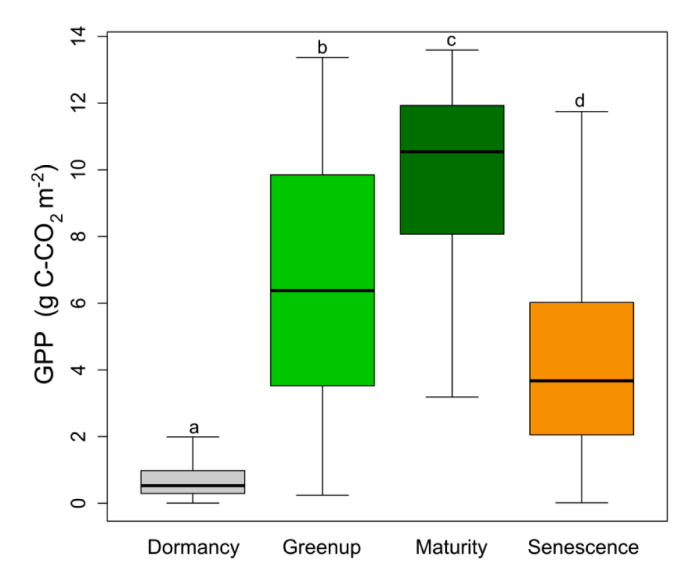


Fig. 3. Daily GPP for each canopy phenological phase during the study period. The gray boxplot represents GPP during Dormancy; the green boxplot represents GPP during Greenup; the dark green boxplot represents GPP during Maturity; the orange boxplot represents GPP during Senescence. Different letters represent significant differences between canopy phenological phases.

contrast, during Dormancy, some samples did not show a decreased reflectance on the FL (Fig. 4h).

3.3. Relationship of VIs and SIF with GPP

We tested the relationship of GPP across the annual cycle and canopy phenological phases with 12 VIs. We found linear relationships between almost all VIs and GPP across the annual cycle, except for $PRI_{(t)}$ and MCARI (Table 2; Supplementary Material (SM) Fig. S2). GPP during Greenup showed relationships with almost all VIs (n=11) (SM Fig. S3), while GPP during Maturity and Dormancy showed relationships with 3 and 1 VIs, respectively (SM Figs. S4 and S6, respectively). GPP across Senescence showed relationships with 6 VIs (Table 2; SM Fig. S5). All vegetation indices, except MCARI and PSRI, showed a positive slope

with GPP across the annual cycle and for each canopy phenological phase. We found that PSRI was the only VIs that showed a relationship with GPP across all canopy phenological phases with a linear model (Table 2; Fig. 5). Because of the pattern of this data, we added a test of an exponential decay model between PSRI and GPP (Fig. 5).

Results from the stepwise regression models for annual GPP, including the dormancy phase (i.e., Annual(wd)) and not including dormancy (i.e., Annual(nd)), are presented in supplementary materials Table S1. This table shows that VIs explained 87% of the GPP annual variability, and the most relevant were GCC, SIF, and CI-Green. Furthermore, to test the influence of VIs different than GCC, we removed this index and found that GPP annual variability was explained by at least 84%, and the most relevant indices were RedEdge-NDVI-a, CI-Green, and CI-RedEdge (SM Table S1).

3.4. Data-model agreement of GPP with different electromagnetic regions across canopy phenological phases

For the electromagnetic regions of VIS-IR, IR and RedEdge, we found a good data-model agreement between GPP and reflectance for model calibration for the scenarios of Annual $_{(\text{MD})}$ (r^2 =0.78 to 0.83), Annual $_{(\text{nD})}$ (r^2 =0.74 to 0.83), and Greenup (r^2 =0.54 to 0.86; Table 3). We did not find a robust data-model agreement between GPP and reflectance for any electromagnetic regions analyzed during Maturity, Senescence, and Dormancy (i.e., r^2 < 0.2). For this reason, these results are not shown.

Data-model agreement for GPP and reflectance during the annual cycle was higher for Annual $_{\rm (wD)}$ for the VIS-IR electromagnetic region, with a model calibration (i.e., Cal.) of Cal.r²=0.83 (RMSE <1.59 and Bias=-0.02), and a model validation of (i.e., Val.) Val.r²=0.80 (RMSE <1.93 and Bias=0.31). We found similar results for Annual $_{\rm (nD)}$, for the RedEdge electromagnetic region, with a model calibration of Cal. $\rm r^2=0.83$ (RMSE <1.52 and Bias=0.04) and a model validation of Val. $\rm r^2=0.56$ (RMSE <2.35 and Bias=1.29). Greenup showed the best data-model agreement between GPP and reflectance for the RedEdge electromagnetic region, with a model calibration of Cal.r²=0.86 (RMSE <1.40 and Bias=-0.05) and a model validation of Val.r²=0.75 (RMSE <1.40 and Bias=-0.94) (Table 3).

We used correlation analyses to identify the relationship of GPP with reflectance by nanometer for each electromagnetic region (i.e., VIS-IR, IR, RedEdge, and SIF) and scenarios tested with the PLSR approach.

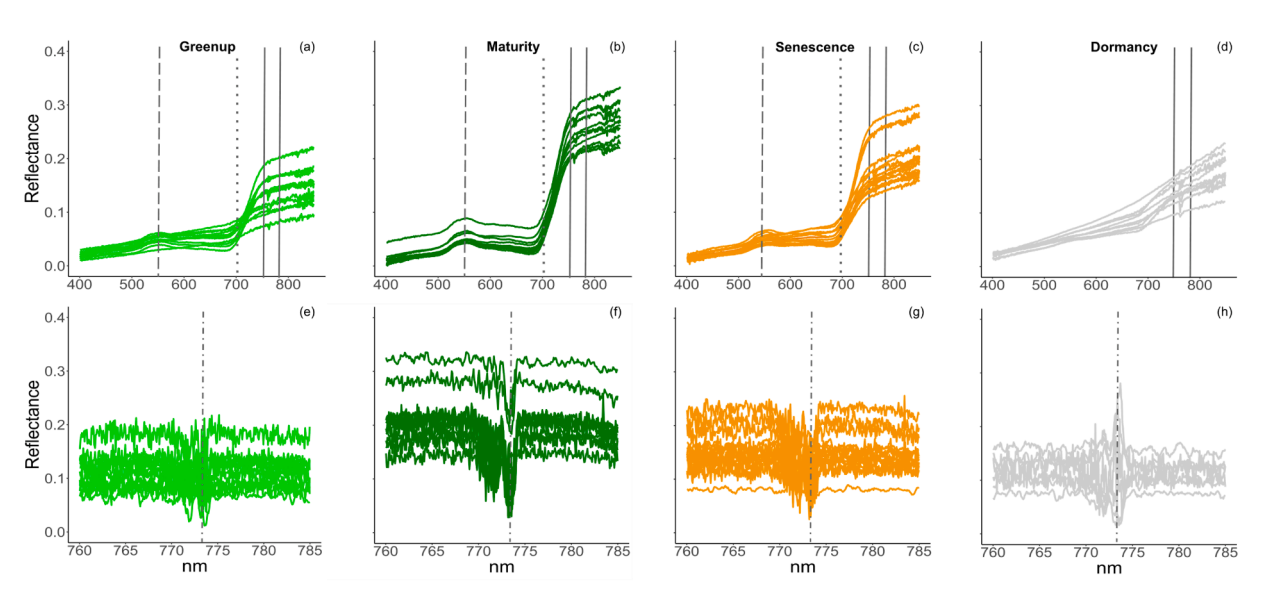


Fig. 4. Hyperspectral reflectance in the Visible and Infrared electromagnetic regions (VIS-IR, a to d) and reflectance in the Sun-Induced Fluorescence (SIF) electromagnetic region (e to h). In all panels, green represents Greenup; dark green represents Maturity; orange represents Senescence; and gray represents Dormancy. For panels a to d, hyphen lines in gray highlight the region of \sim 550 nm, dot lines in gray highlight the region of \sim 700 nm, and vertical solid dark lines highlight the SIF region on panels e to h. For panels e to h, hyphen-dot lines highlight the region of 773.5 nm.

We found different correlation coefficients between GPP and reflectance across the electromagnetic regions (Fig. 6a–c). As expected, our results showed that GPP followed a similar response to vegetated coverage for the VIS-IR electromagnetic region (Fig. 6a); this means a small peak in the green region, a decrease in the red region, and an increase in the IR region. GPP and reflectance correlation coefficients across the IR region for the scenarios were positive and similar (r > 0.6; Fig. 6b), while GPP and reflectance correlation coefficients across the RedEdge region were negative before 715 nm and positive after 720 nm (Fig. 6c).

To identify the contribution of each nanometer on the overall prediction variance of GPP across different scenarios for each PLSR model, we found that VIP showed differences between the data-model agreement of GPP and reflectance across the electromagnetic regions (Fig. 7). VIP for the VIS-IR region showed the most contrasting pattern across canopy phenological phases, with higher differences \sim 550 nm, \sim 720 nm, and \sim 770 nm (Fig. 7a). VIP for the IR region and for the RedEdge region showed a similar pattern and values for the scenarios (Fig. 7b and Fig. 7c; respectively).

4. Discussion

4.1. Reflectance from hyperspectral PRS during canopy phenological phases

Our results showed significant differences in GPP across the annual cycle and for almost all canopy phenological phases. Maturity showed ~133% higher daily GPP than the daily annual cumulative GPP; in contrast, daily cumulative GPP during Dormancy was ~83% lower than the daily annual cumulative GPP (Fig. 3). These changes across the annual cycle influenced the reflectance as a response to changes in the physical structure of grasses, the increase of greenness (or a shift of greenness to brownness), the reabsorption of nutrients, and the influence of soil (Vazquez-Lule, et al. 2022). These changes increase the reflectance when grasses decay during senescence and throughout the dormancy phase (Jacquemoud and Ustin, 2019; Matthes et al., 2015; Xiao et al., 2019).

We highlight the spectral difference between the use of GCC to identify canopy phenological phases during the study period and the pattern identified with the hyperspectral PRS during the transition of Maturity to Senescence in 2017 (i.e., spectral samples that were identified as part of senescence but they had a hyperspectral pattern that matched better the samples of maturity). Maturity during 2017 was at least 50% shorter in duration than the same phase during other years (Fig. 2a), resulting in an abrupt transition to Senescence. The consequence of this rough transition is that two samples from early August 2017 were assigned to Senescence with the GCC (i.e., Fig. 4c; samples with higher reflectance), but the reflectance measured with the hyperspectral PRS resembled samples from the Maturity phase (Fig. 4b). We attribute these differences to the ability of the hyperspectral data to explain broad differences in the greenness condition of vegetation (i.e., before the 700 nm) and changes related to the physiological activity of vegetation, that are better captured by the IR region after the 700 nm (Peñuelas and Filella, 1998).

4.2. Role of VIs to model GPP in salt marsh ecosystems

Our results showed that almost all VIs considered in this study could model GPP across the annual cycle (Table 2). We attribute this finding to two reasons: (a) better performance of regression models with more data, and (b) higher representativeness of the GPP variability during the annual cycle. The GCC derived from PhenoCam showed higher significant relationships (i.e., r^2 =0.81); this result is consistent with studies in salt marshes that found an association between GCC and the net ecosystem productivity and GPP (Hill et al., 2021; Knox et al., 2017). The functionality of GCC to model GPP could relate to the spatial coverage of regions of interest (i.e., ROI's) from the PhenoCam data that

Table 2Linear regression models between VIs and GPP across the annual cycle and by canony phenological phases over three years in a salt marsh.

Vegetation Indices	GPP g C-CO ₂ m ⁻²						
	Annual Slope (r ²)	Greenup Slope (r ²)	Maturity Slope (r ²)	Senescence Slope (r ²)	Dormancy Slope (r ²)		
NDVI _(t)	16.9	18.5		13.4 (0.32)*			
	(0.75)*	(0.79)*					
GCC Index _(p)	140.9	163	129	115.7			
	(0.81)*	(0.71)*	(0.30)*	(0.58)*			
SIF	9.9						
	(0.37)*						
CI	25.2	30.1		21 (0.36)*			
	$(0.77)^*$	(0.98)*					
CI-Green	73.8	141.9					
	(0.55)*	(0.90)*					
CI-RedEdge	83.4	132.2		82.8 (0.36)*			
	(0.74)*	(0.95)*					
EVI	33.4.2	49.84					
	(0.62)*	(0.87)*					
MCARI		-553.9					
		(0.98)*					
PSRI	-35	-37.7	-79.4	-26.4 (0.39)	-8.8 (0.78)		
	(0.75)*	(0.92)*	(0.60)*	*	*		
RedEdge-	29.1	34.4		22.3 (0.30)*			
NDVI-a	$(0.77)^*$	(0.98)*					
RedEdge-	43.1	49.4					
NDVI-b	$(0.78)^*$	(0.96)*					
sPRI	3131.8	4685.9	3190.4				
	(0.63)*	(0.72)*	(0.60)*				

 $^{^{*}}$ Significant differences (p < 0.05). Table does not show relationships between VI's and GPP lower than $\rm r^2$ <0.3.

 $NDVI_{(t)}$: Normalized Difference Vegetation Index; PRI: Photochemical Reflectance Index; GCC Index $_{(p)}$: Greenness Index; SIF: Sun-Induced Fluorescence; CI: Chlorophyll Index; CI-Green: Chlorophyll Index of Green; CI-RedEdge: Chlorophyll Index of Red Edge; EVI: Enhanced Vegetation Index; GCC: Greenness Index; MCARI: Modified chlorophyll absorption ratio index; PSRI: Plant Senescence Reflectance Index; RedEdge-NDVI-a: Red Edge Normalized Difference vegetation Index (use of 710 nm); RedEdge-NDVI-b: Red Edge Normalized Difference vegetation Index (use of 720 nm); sPRI: Modified Photochemical Reflectance Index.

Panel figures of these relationships are in SM Figs. S2 to S6.

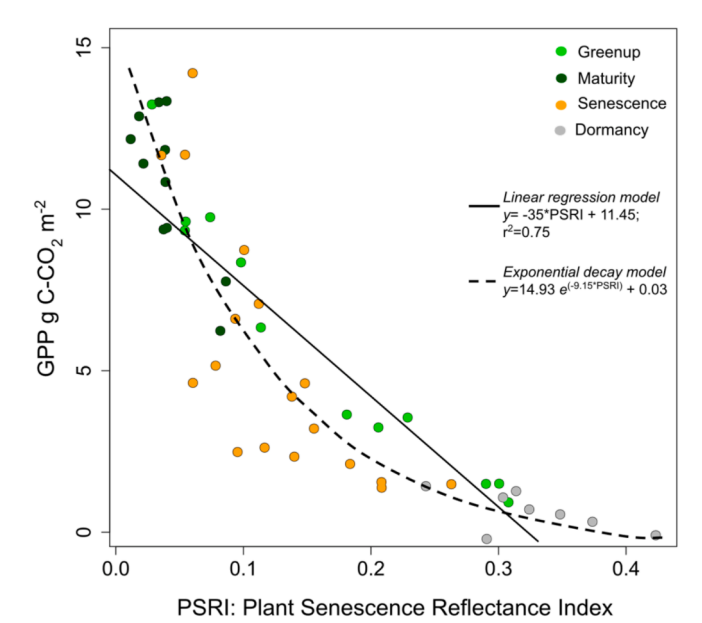


Fig. 5. Linear regression and exponential decay models between the Plant Senescence Reflectance Index (PSRI) and GPP across the canopy phenological phases.

⁽t) Sensors installed on the Eddy Covariance Tower.

⁽p) VI derived from PhenoCam data.

Table 3
Data-model agreement of GPP and reflectance analyzed with the PLSR approach.

Reflectance Electromagnetic Region	Model Fitting for GPP	n	Components	Model Calibration		Model Validation			
				\mathbf{r}^2	RMSE *	BIAS	r ²	RMSE *	BIAS
480 to 820 nm	Annual (wD)	42	3	0.83	1.59	-0.02	0.80	1.93	0.31
VIS-IR	Greenup	12	3	0.81	1.61	-0.06	0.64	1.54	0.10
	Annual (nD)	36	3	0.74	2.16	-0.12	0.92	0.75	0.27
756 to 820 nm. InfraRed	Annual (wD)	42	2	0.78	1.79	0.02	0.91	1.22	-0.14
	Greenup	12	4	0.54	2.43	-0.33	0.46	1.89	0.67
	Annual (nD)	36	3	0.80	1.66	0.07	0.88	1.52	0.46
675 to 755 nm.	Annual (wD)	43	5	0.79	1.75	0.23	0.75	2.14	0.33
Red Edge	Greenup	12	2	0.86	1.40	-0.05	0.75	1.27	-0.94
	Annual (nD)	36	4	0.83	1.52	0.04	0.56	2.35	1.29

^{*} RMSE is in g C-CO₂ m⁻²; (wD) With Dormancy; (nD) Without Dormancy.

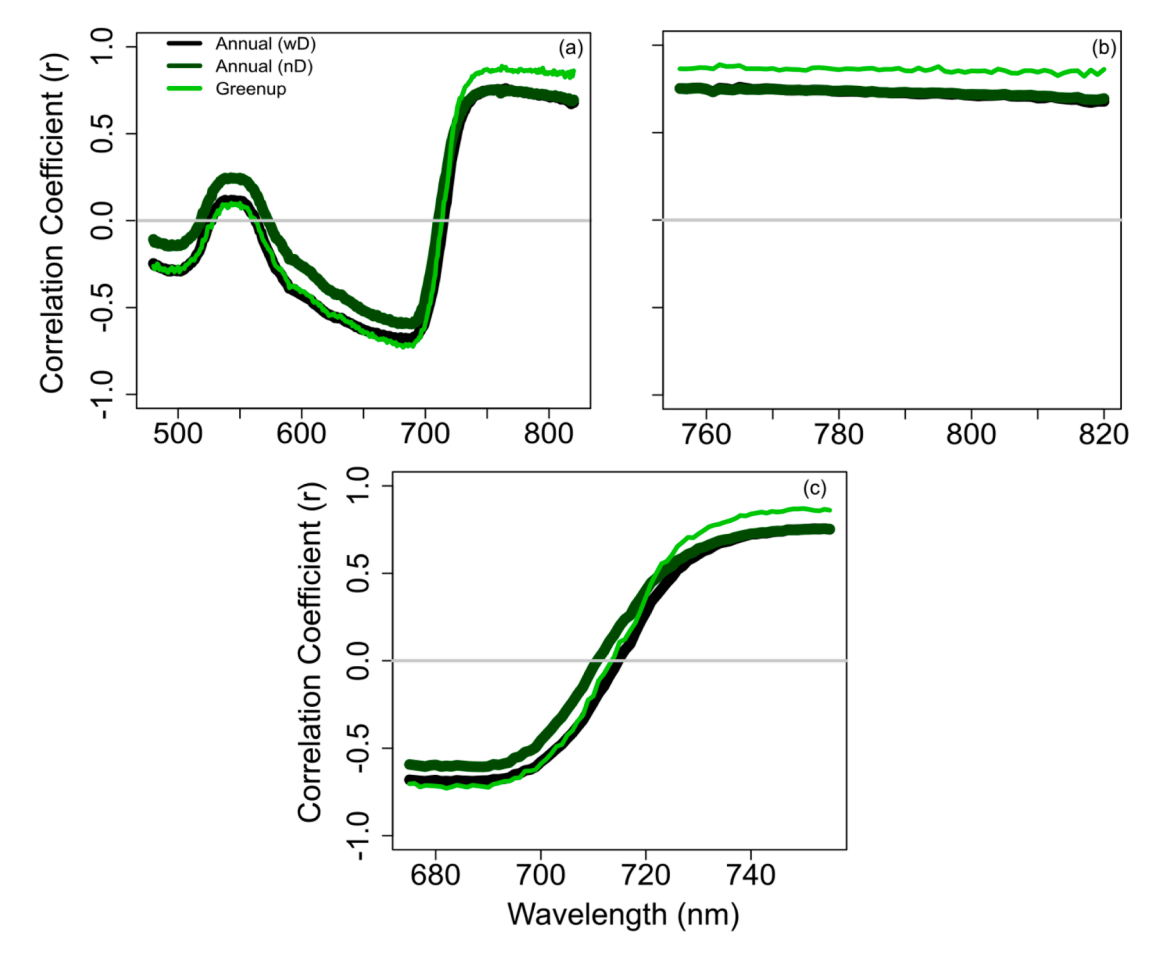


Fig. 6. Summary of correlation coefficients between GPP and reflectance for each nanometer across different electromagnetic regions. (a) Correlation coefficients between GPP and reflectance from 480 to 820 nm (Visible and infrared region); (b) Correlation coefficients between GPP and reflectance from 756 to 820 nm (Infrared region); (c) Correlation coefficients between GPP and reflectance from 675 to 755 nm (RedEdge region).

can represent a broad canopy response from dominant species in the ecosystem, even higher than ROI's collected from the hyperspectral PRS sensors and automatic spectral sensors (i.e., NDVI(t) and PRI (t)) (Hill et al., 2021). In addition, GCC is formulated from the intensity of primary colors instead of the reflectance (Richardson, 2019); this could reduce the influence of atmospheric conditions on the responses. Results about the relationship between PhenoCam data and GPP are consistent with findings in salt marshes and other ecosystems (Filippa et al., 2018; Hill et al., 2021; Knox et al., 2017). Our stepwise results also show that a couple of VIs could help model annual GPP (SM Table S1) and that the most relevant VIs were those more sensitive to changes in the greenness condition.

Almost all VIs had a higher relationship with GPP during the

Greenup canopy phenological phase than other phases (i.e., $\rm r^2$ =0.71 to 0.98). We attribute this finding to the dynamic increase and range of greenness and the development of grasses during this time, characterized by a positive slope on the GPP curve (Fig. 2e). This GPP signature during Greenup may favor the linear relationship with almost all VIs (Table 2). This also could be related to the wavelengths used to formulate the VIs, which are most sensitive to identifying changes in the chlorophyll concentration that influence photosynthesis activity. Consequently, all the indices used in this study considered the red region of the electromagnetic spectrum (\sim 620 to \sim 740 nm, Table 2) related to energy absorption by chlorophyll pigments. In addition, 50% of these indices used the green region (\sim 500 to 570 nm). The reflectance in this part of the electromagnetic spectrum increases with photosynthesis

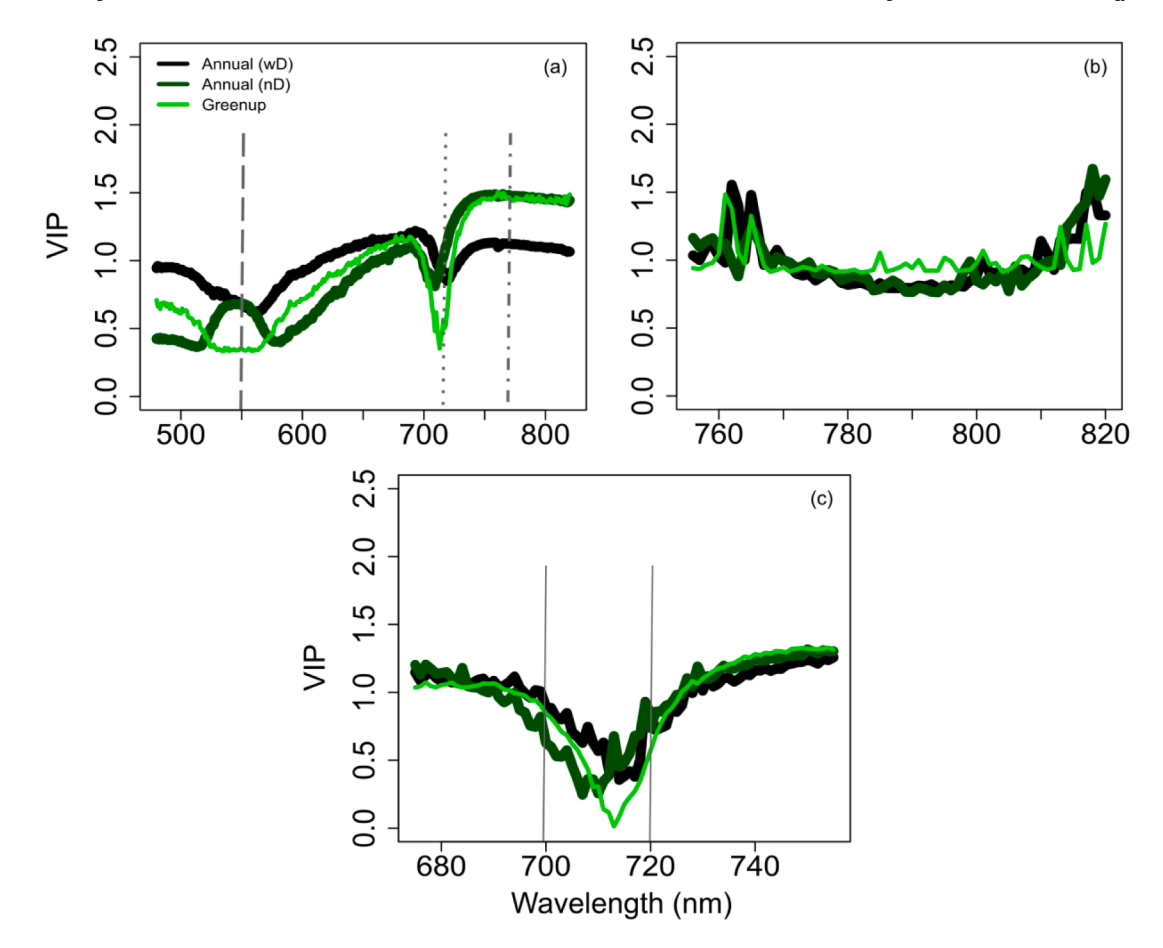


Fig. 7. Summary of Variable Importance of Projection (VIP) for GPP for different electromagnetic regions and canopy phenological phases. (a) VIP between GPP and reflectance from 480 to 820 nm (VIS-IR), the hyphened line highlights the region of \sim 550 nm, the dotted line the region of \sim 720 nm, and the hyphen-dotted line the region of \sim 770 nm; (b) VIP between GPP and reflectance from 756 to 820 nm (IR); (c) VIP between GPP and reflectance from 675 to 755 nm (RedEdge); the solid lines represent the region with higher contrast that is \sim 700 nm to \sim 720 nm.

rates during the active growth of grasses (Jacquemoud and Ustin, 2019). For the rest of the canopy phenological phases, the relationships between GPP and VIs showed a lower r² (i.e., 0.71). During Maturity, the sensitivity of VIs is reduced due to the possibility of sensor oversaturation caused by the complete soil coverage by green vegetation in the field (Jacquemoud and Ustin, 2019), as well as consistent growth of grasses during this phenophase. We highlight that environmental conditions during Maturity, particularly the amount of light (i.e., high values of PAR, Fig. 2b), may interfere with the hyperspectral collections (Brantley et al., 2011; Gnyp et al., 2014). We also found a less strong relationship between VIs and GPP across Senescence (Table 2; r²=0.30 to 0.58). We attribute this response to the combined influence of active vegetation (i.e., green grasses still growing) and less physiologically active foliage (i.e., turn on from green to brown grasses), as well as the defoliation of grasses and an increasing exposition of soils. For the lack of relationship of VIs with GPP across Dormancy, we attribute this finding to the lower GPP values as a response of inactive vegetation during that phase (Fig. 3), as a consequence of a reduction of photosynthetic pigments that influence the response of vegetation indices across other phenological phases; in addition, an increase of soil response and dead vegetation may oversaturate the reflectance in this part of the electromagnetic spectrum (Xiao et al., 2019; Zhu et al., 2010).

Our results showed that PSRI could model GPP across the annual cycle and all canopy phenological phases (Table 2; Fig. 5). The PSRI index was initially formulated to follow changes in the chlorophyll-carotenoid ratio (i.e., Chl/Car) (Merzlyak et al., 1999). Recent studies in terrestrial grasses have found that PSRI showed a higher relationship

with GPP across phenological phases, mainly because of its sensitivity to detect changes in the pigments' concentration, rapid changes in the decay of chlorophyll, and the increase of carotenoids (Cerasoli et al., 2018; Merzlyak et al., 2003). Increases in PSRI values could be indirectly related to transitions in canopy phenology and their impact on photosynthesis, ultimately affecting GPP (Gamon, 2015). This result is also supported by the relationship of GPP with the sPRI, which was also formulated to follow up changes on the Chl/Car ratio (Gamon et al., 1992). However, this result contrasts with the lack of relationship between $\mbox{PRI}_{(t)}$ and \mbox{GPP} (Table 2). Similar findings have been reported due to a decrease in the sensitivity of the PRI to changes in the canopy structure, particularly the leaf inclination angle at the stand-level (Gitelson et al., 2017a, 2017b). We also attributed this finding to the ROI's collected by automatic spectral sensors, which represent less variability of the salt marsh ecosystem because of their constant monitoring at the same area compared with a larger representation of the spatial variability with hyperspectral collections (samples collected in an area of 450 m²).

In addition, we found an exponential decay of GPP with the PSRI; this finding could be an indirect response of vegetation to the increase of non-photosynthetic water-soluble pigments, such as anthocyanins, that are associated with the resistance of vegetation when stress in the environment increases (Jacquemoud and Ustin, 2019; Vina and Gitelson, 2011). In our study site, a decrease in solar radiation could be associated with low air temperature at the end of the year (i.e., canopy phenological phases of senescence and dormancy) associated with a decrease in GPP.

Contrary to our expectations, we did not find a strong linear

relationship between SIF and GPP (Table 2, supplementary materials Fig. S2c). We attribute these results to several possibilities: (a) the angle and influence of incident light on the vegetation during the data collections (Zhang et al., 2021); (b) the daily scale of our approach, which limits our understanding of the relationship between GPP and SIF during the diurnal cycle; and (c) changes in the canopy structure and the influence of shaded and sunlight leaves on the absorbed photosynthetically active radiation (APAR). This last point has been suggested as one of the main drivers of the positive relationships between SIF and GPP (Dechant et al., 2020; Yang et al., 2021). We highlight that SIF had negative values during the early growing season (i.e., early Greenup) and the end of the growing season (i.e., Dormancy). Similar results have been found in bare soils or where vegetation is scarce as an artificial response because of an oversaturation of the sensors (Turner et al., 2020). Our results are consistent with recent research developed for crops. However, we postulate that additional information combining SIF, GPP, and APAR is needed for salt marshes across the diurnal cycle to understand limitations and opportunities to model GPP from SIF at the canopy scale and with satellite sources across different canopy phenological phases.

4.3. Data-model agreement between GPP and reflectance with the PLSR approach

Our findings for the data model agreement between GPP and reflectance from the VIS-IR region with the PLSR approach showed a better performance across the annual cycle and during the Greenup canopy phenological phase (Table 3). We attributed this finding to the availability of all spectra to model the vegetation response, such as the structural changes on the canopy and the greenness condition of vegetation (Fig. 6a).

It is expected that the IR region responds to changes in the physiological conditions of vegetation, particularly as a response to the water content of the leaves (Peñuelas and Filella, 1998). However, the IR region was less sensitive to model GPP changes in this ecosystem with the PLSR approach. This could be related to the differences in the short-range covered by our hyperspectral sensors (~700 nm to 820 nm) compared with the full coverage of the IR region (~700 nm to 1000 nm). Consequently, it is possible that this technical limitation may constrain our findings, and future studies should consider hyperspectral sensors capable of measuring the whole IR region to model GPP. We advocate for more studies using hyperspectral measurements in salt marshes to represent how changes in nutrients and photosynthesis influence the reflectance of canopy dynamics (Vazquez-Lule et al., 2022).

Our results suggest that additional information in the electromagnetic region (i.e., VIS-IR) is relevant to model and predicting GPP in this temperate salt marsh but may not be essential to predicting GPP in other ecosystems. For example a study in a subalpine evergreen forest did not find improvement in modeling GPP using the entire electromagnetic region when compared with the specific use of VIs (Cheng et al., 2020). Instead of reflectance, we propose that different approaches (e.g., radiances) could be tested to improve the data-model agreement of GPP across other canopy phenological phases in salt marsh grasses with the PLSR approach (Dechant et al., 2019). Hyperspectral information is flexible and has multiple possibilities for analyzing different regions of the electromagnetic spectrum. For example, there is a large potential for indices that could minimize the influence of soils background and could potentially increase the accuracy of estimating GPP across different environmental conditions (e.g., NIRv and NIRvP; Badgley et al. 2017, Dechant et al. 2022). It is also relevant to use the thermal infrared to model and test the relationship between photosynthesis and other physiological processes such as transpiration (Bayat et al., 2018). Remote sensing thermal information is available from public historical sources (i.e., Landsat, MODIS) and future missions that will have improvements on the spectral and spatial resolution (e.g., the Surface Biology and Geology from the USGS, Environmental Monitoring and

Analysis Program from the German Space Agency mission (EnMAP) (Ustin and Middleton, 2021)).

We highlight challenges related to differences in the spatial and temporal scale related to collecting PRS information and GPP. While GPP represents information at the ecosystem scale, including the footprint areas of the PRS sensors, it has a higher temporal variability than that measured with PRS. Future studies could use PSR aided by drones or airborne sensors to cover a larger area within the footprint of an EC tower. Furthermore, GPP represents integrated measurements at the daily scale, which has a temporal overlap with collections from the automatic spectral sensors and the PhenomCam but not the hyperspectral reflectance (i.e., collected for ~ 1.5 weeks). This temporal mismatch may impact the modeling performance using different electromagnetic regions and VIs, and the limitation to identify changes in canopy phenological stages with hyperspectral information. We suggest that future studies may use automatic and synchronized measurements of hyperspectral information and GPP to improve modeling efforts (Woodgate et al., 2020; Zarco-Tejada et al., 2013)

5. Conclusions

Our results highlight the challenges of modeling and predicting GPP with PRS in a temperate tidal salt marsh with high variability during the annual cycle as a response to different canopy phenological phases. We also showed that VIs related to Chl/Car ratio changes were more valuable to model GPP across almost all canopy phenological phases than VIs formulated with reflectance data from the IR region. In addition, the hyperspectral VIS-IR region showed more sensitivity to improve the data-model agreement of GPP with the PLSR approach across the annual cycle. We also highlighted differences in the usability of other PRS instruments (i.e., PhenoCam, Spectral sensors, and Hyperspectral PRS) to generate information that can model GPP, particularly differences in the footprint of every sensor, type of collection (i.e., manual vs. automatic) and temporal frequency. We conclude that this salt marsh shows essential differences among phenological canopy phases that influence the performance of reflectance and VIs to model and predict GPP. These results demonstrate the potential to model and predict the annual variability of GPP in a salt marsh ecosystem with conventional vegetation indices and the hyperspectral data from the VIS-IR region.

CRediT authorship contribution statement

Alma Vázquez-Lule: Conceptualization, Data curation, Formal analysis, Methodology, Writing – review & editing. **Rodrigo Vargas:** Conceptualization, Methodology, Resources, Writing – review & editing.

Declaration of Competing Interest

The authors declare the following financial interests/personal relationships which may be considered as potential competing interests:

Rodrigo Vargas reports financial support was provided by National Science Foundation. RV is a guest editor for the VSI AmeriFlux 25 for the journal to which this manuscript is submitted.

Data availability

EC data for the study site are publicly available *via* AmeriFlux available online https://ameriflux.lbl.gov/sites/siteinfo/US-StJ#ov erview. Hyperspectral and leaf nutrients data, as well the PLSR model outputs are publicly available *via* Ecosis available online https://ecosis.org/package/hyperspectral-data-for-measuring-vegetation-nutrients-and-canopy-photosynthesis-in-a-salt-marsh.

Acknowledgments

AVL acknowledges support from the National Council for Science and Technology (CONACYT, Mexico; fellowship #240634/440832), the Delaware Environmental Graduate Fellowship (DENIN) and the John A. Knauss Marine Policy Fellowship, Global Ocean Monitoring and Observing Program and Sea Grant Program, NOAA. RV acknowledges support from the National Science Foundation (#1652594). The authors are grateful for the onsite support from the Delaware National Estuarine Research Reserve (DNERR). The authors acknowledge the land they realized this study as the traditional home of the Lenni-Lenape tribal nation (Delaware nation). This manuscript was improved with constructive feedback from two anonymous reviewers.

Supplementary materials

Supplementary material associated with this article can be found, in the online version, at doi:10.1016/j.agrformet.2023.109639.

References

- Adam, E., Mutanga, O., Rugege, D., 2010. Multispectral and hyperspectral remote sensing for identification and mapping of wetland vegetation: a review. Wetl. Ecol. Manag. 18, 281–296.
- Alongi, D.M., 2020. Carbon balance in salt marsh and mangrove ecosystems: a global synthesis. J. Mar. Sci. Eng. 8, 767.
- Asner, G.P., Martin, R.E., 2016. Spectranomics: emerging science and conservation opportunities at the interface of biodiversity and remote sensing. Global Ecol. Conserv. 8, 212–219.
- Badgley, G., Field, C.B., Berry, J.A., 2017. Canopy near-infrared reflectance and terrestrial photosynthesis. Sci. Adv. 3, e1602244.
- Bayat, B., van der Tol, C., Verhoef, W., 2018. Integrating satellite optical and thermal infrared observations for improving daily ecosystem functioning estimations during a drought episode. Remote Sens. Environ. 209, 375–394.
- Brantley, S.T., Zinnert, J.C., Young, D.R., 2011. Application of hyperspectral vegetation indices to detect variations in high leaf area index temperate shrub thicket canopies. Remote Sens. Environ. 115, 514–523.
- Capooci, M., Barba, J., Seyfferth, A.L., Vargas, R., 2019. Experimental influence of stormsurge salinity on soil greenhouse gas emissions from a tidal salt marsh. Sci. Total Environ. 686, 1164–1172.
- Cerasoli, S., Campagnolo, M., Faria, J., Nogueira, C., Caldeira, M., da, C., 2018. On estimating the gross primary productivity of Mediterranean grasslands under different fertilization regimes using vegetation indices and hyperspectral reflectance. Biogeosciences 15, 5455–5471.
- Cheng, R., Magney, T.S., Dutta, D., Bowling, D.R., Logan, B.A., Burns, S.P., Blanken, P.D., Grossmann, K., Lopez, S., Richardson, A.D., Stutz, J., Frankenberg, C., 2020. Decomposing reflectance spectra to track gross primary production in a subalpine evergreen forest. Biogeosciences 17, 4523–4544.
- Dechant, B., Ryu, Y., Badgley, G., Köhler, P., Rascher, U., Migliavacca, M., Zhang, Y., Tagliabue, G., Guan, K., Rossini, M., Goulas, Y., Zeng, Y., Frankenberg, C., Berry, J. A., 2022. NIRVP: a robust structural proxy for sun-induced chlorophyll fluorescence and photosynthesis across scales. Remote Sens. Environ. 268, 112763.
- Dechant, B., Ryu, Y., Badgley, G., Zeng, Y., Berry, J.A., Zhang, Y., Goulas, Y., Li, Z., Zhang, Q., Kang, M., Li, J., Moya, I., 2020. Canopy structure explains the relationship between photosynthesis and sun-induced chlorophyll fluorescence in crops. Remote Sens. Environ. 241. https://doi.org/10.1016/j.rse.2020.111733.
- Dechant, B., Ryu, Y., Kang, M., 2019. Making full use of hyperspectral data for gross primary productivity estimation with multivariate regression: mechanistic insights from observations and process-based simulations. Remote Sens. Environ. 234, 111435.
- Delwiche, K.B., Knox, S.H., Malhotra, A., Fluet-Chouinard, E., McNicol, G., Feron, S., Ouyang, Z., Papale, D., Trotta, C., Canfora, E., Cheah, Y.-W., Christianson, D., Alberto, M.C.R., Alekseychik, P., Aurela, M., Baldocchi, D., Bansal, S., Billesbach, D. P., Bohrer, G., Bracho, R., Buchmann, N., Campbell, D.I., Celis, G., Chen, J., Chen, W., Chu, H., Dalmagro, H.J., Dengel, S., Desai, A.R., Detto, M., Dolman, H., Eichelmann, E., Euskirchen, E., Famulari, D., Fuchs, K., Goeckede, M., Gogo, S., Gondwe, M.J., Goodrich, J.P., Gottschalk, P., Graham, S.L., Heimann, M., Helbig, M., Helfter, C., Hemes, K.S., Hirano, T., Hollinger, D., Hörtnagl, L., Iwata, H., Jacotot, A., Jurasinski, G., Kang, M., Kasak, K., King, J., Klatt, J., Koebsch, F., Krauss, K.W., Lai, D.Y.F., Lohila, A., Mammarella, I., Belelli Marchesini, L., Manca, G., Matthes, J.H., Maximov, T., Merbold, L., Mitra, B., Morin, T.H., Nemitz, E., Nilsson, M.B., Niu, S., Oechel, W.C., Oikawa, P.Y., Ono, K., Peichl, M., Peltola, O., Reba, M.L., Richardson, A.D., Riley, W., Runkle, B.R.K., Ryu, Y., Sachs, T., Sakabe, A., Sanchez, C.R., Schuur, E.A., Schäfer, K.V.R., Sonnentag, O., Sparks, J.P., Stuart-Haëntjens, E., Sturtevant, C., Sullivan, R.C., Szutu, D.J., Thom, J.E., Torn, M.S., Tuittila, E.-S., Turner, J., Ueyama, M., Valach, A.C., Vargas, R., Varlagin, A., Vazquez-Lule, A., Verfaillie, J.G., Vesala, T., Vourlitis, G.L., Ward, E.J., Wille, C., Wohlfahrt, G., Wong, G.X., Zhang, Z., Zona, D., Windham-Myers, L., Poulter, B., Jackson, R.B., 2021, FLUXNET-CH4: a global, multi-ecosystem dataset and analysis of methane seasonality from freshwater wetlands. Earth Syst. Sci. Data Discuss. 13, 3607-3689.

- DuBois, S., Desai, A.R., Singh, A., Serbin, S.P., Goulden, M.L., Baldocchi, D.D., Ma, S., Oechel, W.C., Wharton, S., Kruger, E.L., Townsend, P.A., 2018. Using imaging spectroscopy to detect variation in terrestrial ecosystem productivity across a water-stressed landscape. Ecol. Appl. 28, 1313–1324.
- Eagin, R.A., Forbrich, I., Huff, T.P., Barr, J.G., Ruiz-Plancarte, J., Fuentes, J.D., Najjar, R. G., Vargas, R., Vázquez-Lule, A., Windham-Myers, L., Kroeger, K.D., Ward, E.J., Moore, G.W., Leclerc, M., Krauss, K.W., Stagg, C.L., Alber, M., Knox, S.H., Schäfer, K. V.R., Bianchi, T.S., Hutchings, J.A., Nahrawi, H., Noormets, A., Mitra, B., Jaimes, A., Hinson, A.L., Bergamaschi, B., King, J.S., Miao, G., 2020. Tidal wetland gross primary production across the continental United States. Glob. Biogeochem. 34, 2000–2019.
- Filippa, G., Cremonese, E., Migliavacca, M., Galvagno, M., Forkel, M., Wingate, L., Tomelleri, E., Morra, U., Richardson, A.D., 2016. Agricultural and forest meteorology phenopix: a R package for image-based vegetation phenology. Agric. For. Meteorol. 220, 141–150.
- Filippa, G., Cremonese, E., Migliavacca, M., Galvagno, M., Sonnentag, O., Humphreys, E., Hufkens, K., Ryu, Y., Verfaillie, J., Morra di Cella, U., Richardson, A.D., 2018. NDVI derived from near-infrared-enabled digital cameras: applicability across different plant functional types. Agric. For. Meteorol. 249, 275–285.
- Forbrich, I., Giblin, A.E., Hopkinson, C.S., 2018. Constraining marsh carbon budgets using long-term C burial and contemporary atmospheric CO₂ fluxes. J. Geophys. Res. Biogeosci. 123, 867–878.
- Gamon, J.A., 2015. Reviews and Syntheses: optical sampling of the flux tower footprint. Biogeosciences 12, 4509–4523.
- Gamon, J.A., Kovalchuck, O., Wong, C.Y.S., Harris, A., Garrity, S.R., 2015. Monitoring seasonal and diurnal changes in photosynthetic pigments with automated PRI and NDVI sensors. Biogeosciences 12, 4149–4159.
- Gamon, J.A., Peñuelas, J., Field, C.B., 1992. A narrow-waveband spectral index that tracks diurnal changes in photosynthetic efficiency. Remote Sens. Environ. 44, 35–44.
- Gitelson, A., Merzlyak, M.N., 1994. Spectral reflectance changes associated with autumn senescence of Aesculus hippocastanum L. and Acer platanoides L. leaves. Spectral features and relation to chlorophyll estimation. J. Plant Physiol. 143, 286–292.
- Gitelson, A.A., Gamon, J.A., Solovchenko, A., 2017a. Multiple drivers of seasonal change in PRI: implications for photosynthesis 1. Leaf level. Remote Sens. Environ. 191, 110–116.
- Gitelson, A.A., Gamon, J.A., Solovchenko, A., 2017b. Multiple drivers of seasonal change in PRI: implications for photosynthesis 2. Stand level. Remote Sens. Environ. 190, 198–206.
- Gitelson, A.A., Merzlyak, M.N., 1996. Signature analysis of leaf reflectance spectra: algorithm development for remote sensing of chlorophyll. J. Plant Physiol. 148, 494–500.
- Gitelson, A.A., Viña, A., Ciganda, V., Rundquist, D.C., Arkebauer, T.J., 2005. Remote estimation of canopy chlorophyll content in crops. Geophys. Res. Lett. 32, 1–4.
- Gnyp, M.L., Miao, Y., Yuan, F., Ustin, S.L., Yu, K., Yao, Y., Huang, S., Bareth, G., 2014. Hyperspectral canopy sensing of paddy rice aboveground biomass at different growth stages. Field Crops Res. 155, 42–55.
- Gu, L., Post, W.M., Baldocchi, D.D., Black, T.A., Suyker, A.E., Verma, S.B., Vesala, T., Wofsy, S.C., 2009. Characterizing the seasonal dynamics of plant community photosynthesis across a range of vegetation types. Phenology of Ecosystem Processes. Springer, New York, New York, NY, pp. 35–58.
- Hayes, D.J., Vargas, R., Alin, S.R., Conant, R., T. Hutyra, L.H., Jacobson, A.R., Kurz, W. A., Liu, S., McGuire, A.D., Poulter, B., Woodall, C.W., 2018. Chapter 2: The North American carbon budget, in: Cavallaro, N., Shrestha, G., Birdsey, R., Mayes, M.A., Najjar, R.G., Reed, S.C., Romero-Lankao, P. Zhu, Z. (Eds.), Second state of the carbon cycle report (SOCCR2): a sustained assessment report. U.S. Global Change Research Program, Washington, DC, USA, pp. 71–108, 10.7930/SOCCR2.2018.Ch2.
- Hill, A.C., Vázquez-Lule, A., Vargas, R., 2021. Linking vegetation spectral reflectance with ecosystem carbon phenology in a temperate salt marsh. Agric. For. Meteorol. 307, 108481.
- Huete, A., Didan, K., Miura, T., Rodriguez, E.P., Gao, X., Ferreira, L.G., 2002. Overview of the radiometric and biophysical performance of the MODIS vegetation indices. Remote Sens. Environ. 83, 195–213.
- Inoue, Y., Peñuelas, J., Miyata, A., Mano, M., 2008. Normalized difference spectral indices for estimating photosynthetic efficiency and capacity at a canopy scale derived from hyperspectral and CO₂ flux measurements in rice. Remote Sens. Environ. 112. 156–172.
- Jacquemoud, S., Ustin, S., 2019. Leaf Optical Properties. Cambridge University Press, Cambridge, England. https://doi.org/10.1017/9781108686457.
- Kim, J., Ryu, Y., Dechant, B., Lee, H., Kim, H.S., Kornfeld, A., Berry, J.A., 2021. Solar-induced chlorophyll fluorescence is non-linearly related to canopy photosynthesis in a temperate evergreen needleleaf forest during the fall transition. Remote Sens. Environ. 258, 112362.
- Knox, S.H., Dronova, I., Sturtevant, C., Oikawa, P.Y., Matthes, J.H., Verfaillie, J., Baldocchi, D., 2017. Using digital camera and Landsat imagery with Eddy covariance data to model gross primary production in restored wetlands. Agric. For. Meteorol. 237–238, 233–245.
- Li, X., Xiao, J., He, B., 2018. Chlorophyll fluorescence observed by OCO-2 is strongly related to gross primary productivity estimated from flux towers in temperate forests. Remote Sens. Environ. 204, 659–671.
- Lu, W., Xiao, J., Liu, F., Zhang, Y., Liu, C., Lin, G., 2017. Contrasting ecosystem CO₂ fluxes of inland and coastal wetlands: a meta-analysis of eddy covariance data. Glob. Chang. Biol. 23, 1180–1198.
- Malthus, T.J., Mumby, P.J., 2003. Remote sensing of the coastal zone: an overview and priorities for future research. Int. J. Remote Sens. 24, 2805–2815.

- Matthes, J.H., Knox, S.H., Sturtevant, C., Sonnentag, O., Verfaillie, J., Baldocchi, D., 2015. Predicting landscape-scale CO₂ flux at a pasture and rice paddy with long-term hyperspectral canopy reflectance measurements. Biogeosciences 12, 4577–4594.
- Meacham-Hensold, K., Fu, P., Wu, J., Serbin, S., Montes, C.M., Ainsworth, E., Guan, K., Dracup, E., Pederson, T., Driever, S., Bernacchi, C., 2020. Plot-level rapid screening for photosynthetic parameters using proximal hyperspectral imaging. J. Exp. Bot. 71, 2312–2328
- Meroni, M., Rossini, M., Guanter, L., Alonso, L., Rascher, U., Colombo, R., Moreno, J., 2009. Remote sensing of solar-induced chlorophyll fluorescence: review of methods and applications. Remote Sens. Environ. 113, 2037–2051.
- Merzlyak, M.N., Gitelson, A.A., Chivkunova, O.B., Rakitin, V.Y.U., 1999. Non-destructive optical detection of pigment changes during leaf senescence and fruit ripening. Physiol. Plant. 106, 135–141.
- Merzlyak, M.N., Solovchenko, A.E., Gitelson, A.A., 2003. Reflectance spectral features and non-destructive estimation of chlorophyll, carotenoid and anthocyanin content in apple fruit. Postharvest. Biol. Technol. 27, 197–211.
- Miao, G., Guan, K., Yang, X., Bernacchi, C.J., Berry, J.A., DeLucia, E.H., Wu, J., Moore, C. E., Meacham, K., Cai, Y., Peng, B., Kimm, H., Masters, M.D., 2018. Sun-Induced chlorophyll fluorescence, photosynthesis, and light use efficiency of a soybean field from seasonally continuous measurements. J. Geophys. Res. Biogeosci. 123, 610–623.
- Migliavacca, M., Galvagno, M., Cremonese, E., Rossini, M., Meroni, M., Sonnentag, O., Cogliati, S., Manca, G., Diotri, F., Busetto, L., Cescatti, A., Colombo, R., Fava, F., Morra di Cella, U., Pari, E., Siniscalco, C., Richardson, A.D., 2011. Using digital repeat photography and eddy covariance data to model grassland phenology and photosynthetic CO₂ uptake. Agric. For. Meteorol. 151, 1325–1337.
- Peñuelas, J., Filella, L., 1998. Visible and near-infrared reflectance techniques for diagnosing plant physiological status. Trends Plant Sci. 3, 151–156.
- Peterson, P.M., Romaschenko, K., Arrieta, Y.H., Saarela, J.M., 2014. A molecular phylogeny and new subgeneric classification of Sporobolus (Poaceae: Chloridoideae: sporobolinae). Taxon 63, 1212–1243.
- Porcar-Castell, A., Tyystjärvi, E., Atherton, J., Van Der Tol, C., Flexas, J., Pfündel, E.E., Moreno, J., Frankenberg, C., Berry, J.A., 2014. Linking chlorophyll a fluorescence to photosynthesis for remote sensing applications: mechanisms and challenges. J. Exp. Bot. 65, 4065–4095.
- Reichstein, M., Falge, E., Baldocchi, D., Papale, D., Aubinet, M., Berbigier, P., Bernhofer, C., Buchmann, N., Gilmanov, T., Granier, A., Grunwald, T., Havrankova, K., Ilvesniemi, H., Janous, D., Knohl, A., Laurila, T., Lohila, A., Loustau, D., Matteucci, G., Meyers, T., Miglietta, F., Ourcival, J.M., Pumpanen, J., Rambal, S., Rotenberg, E., Sanz, M., Tenhunen, J., Seufert, G., Vaccari, F., Vesala, T., Yakir, D., 2005. On the separation of net ecosystem exchange into assimilation and ecosystem respiration: review and improved algorithm. Glob. Chang. Biol. 11, 1424–1439.
- Richardson, A.D., 2019. Tracking seasonal rhythms of plants in diverse ecosystems with digital camera imagery. New Phytol 222, 1742–1750.
- Rossini, M., Meroni, M., Migliavacca, M., Manca, G., Cogliati, S., Busetto, L., Picchi, V., Cescatti, A., Seufert, G., Colombo, R., 2010. High resolution field spectroscopy measurements for estimating gross ecosystem production in a rice field. Agric. For. Meteorol. 150, 1283–1296.
- Ryu, Y., Berry, J.Á., Baldocchi, D.D., 2019. What is global photosynthesis? History, uncertainties and opportunities. Remote Sens. Environ. 223, 95–114.
- Serbin, S.P., Singh, A., McNeil, B.E., Kingdon, C.C., Townsend, P.A., 2016. Spectroscopic determination of leaf morphological and biochemical traits for northern temperate and boreal tree species. Ecol. Appl. 24, 1651–1669.
- Seyednasrollah, B., Milliman, T., Richardson, A.D., 2019. Data extraction from digital repeat photography using xROI: an interactive framework to facilitate the process. ISPRS J. Photogramm. Remote Sens. 152, 132–144.
- Tao, J., Mishra, D., Cotten, D., O'Connell, J., Leclerc, M., Nahrawi, H., Zhang, G., Pahari, R., 2018. A comparison between the MODIS product (MOD17A2) and a tiderobust empirical GPP model evaluated in a Georgia Wetland. Remote Sens. (Basel) 10, 1831.
- Trifunovic, B., Vázquez-Lule, A., Capooci, M., Seyfferth, A.L., Moffat, C., Vargas, R., 2020. Carbon dioxide and methane emissions from temperate salt marsh tidal creek. J. Geophys. Res. Biogeosci. 125 https://doi.org/10.1029/2019jg005558.
- Turner, A.J., Koehler, P., Magney, T.S., Frankenberg, C., Fung, I., Cohen, R.C., 2020.
 A double peak in the seasonality of California's photosynthesis as observed from space. Biogeosciences 17, 405–422.

- Ustin, S.L., Middleton, E.M., 2021. Current and near-term advances in Earth observation for ecological applications. Ecol. Process 10, 1.
- Vázquez-Lule, A., Seyfferth, A.L., Limmer, M.A., Mey, P., Guevara, M., Vargas, R., 2022. Hyperspectral reflectance for measuring canopy-level nutrients and photosynthesis in a salt marsh. J. Geophys. Res. Biogeosci. 127 https://doi.org/10.1029/ 2022je007088
- Vázquez-Lule, A., Vargas, R., 2021. Biophysical drivers of net ecosystem and methane exchange across phenological phases in a tidal salt marsh. Agric. For. Meteorol. 300, 108309.
- Villarreal, S., Guevara, M., Alcaraz-Segura, D., Brunsell, N.A., Hayes, D., Loescher, H.W., Vargas, R., 2018. Ecosystem functional diversity and the representativeness of environmental networks across the conterminous United States. Agric. For. Meteorol. 262, 423–433.
- Villarreal, S., Vargas, R., 2021. Representativeness of FLUXNET sites across Latin America. J. Geophys. Res. Biogeosci. 126 https://doi.org/10.1029/2020jg006090.
- Vina, A., Gitelson, A.A., 2011. Sensitivity to foliar anthocyanin content of vegetation indices using green reflectance. IEEE Geosci. Remote Sens. Lett. 8, 464–468.
- Ward, N.D., Megonigal, J.P., Bond-Lamberty, B., Bailey, V.L., Butman, D., Canuel, E.A.,
 Diefenderfer, H., Ganju, N.K., Goñi, M.A., Graham, E.B., Hopkinson, C.S.,
 Khangaonkar, T., Langley, J.A., McDowell, N.G., Myers-Pigg, A.N., Neumann, R.B.,
 Osburn, C.L., Price, R.M., Rowland, J., Sengupta, A., Simard, M., Thornton, P.E.,
 Tzortziou, M., Vargas, R., Weisenhorn, P.B., Windham-Myers, L., 2020. Representing
 the function and sensitivity of coastal interfaces in Earth system models. Nat.
 Commun. 11, 2458.
- Wold, S., Sjöström, M., Eriksson, L., 2001. PLS-regression: a basic tool of chemometrics. Chemom. Intellig. Lab. Syst. 58, 109–130.
- Woodgate, W., van Gorsel, E., Hughes, D., Suarez, L., Jimenez-Berni, J., Held, A., 2020. THEMS: an automated thermal and hyperspectral proximal sensing system for canopy reflectance, radiance and temperature. Plant Methods 16, 105.
- Wu, C., Niu, Z., Tang, Q., Huang, W., Rivard, B., Feng, J., 2009. Remote estimation of gross primary production in wheat using chlorophyll-related vegetation indices. Agric. For. Meteorol. 149, 1015–1021.
- Xiao, J., Chevallier, F., Gomez, C., Guanter, L., Hicke, J.A., Huete, A.R., Ichii, K., Ni, W., Pang, Y., Rahman, A.F., Sun, G., Yuan, W., Zhang, L., Zhang, X., 2019. Remote sensing of the terrestrial carbon cycle: a review of advances over 50 years. Remote Sens. Environ. 233. 111383.
- Yang, K., Ryu, Y., Dechant, B., Berry, J.A., Hwang, Y., Jiang, C., Kang, M., Kim, J., Kimm, H., Kornfeld, A., Yang, X., 2018. Sun-induced chlorophyll fluorescence is more strongly related to absorbed light than to photosynthesis at half-hourly resolution in a rice paddy. Remote Sens. Environ. 216, 658–673.
- Yang, P., van der Tol, C., Campbell, P.K.E., Middleton, E.M., 2021. Unraveling the physical and physiological basis for the solar- induced chlorophyll fluorescence and photosynthesis relationship using continuous leaf and canopy measurements of a corn crop. Biogeosciences 18, 441–465.
- Zarco-Tejada, P.J., Morales, A., Testi, L., Villalobos, F.J., 2013. Spatio-temporal patterns of chlorophyll fluorescence and physiological and structural indices acquired from hyperspectral imagery as compared with carbon fluxes measured with eddy covariance. Remote Seps. Environ 133, 102–115.
- Zhang, F., Zhou, G., 2017. Deriving a light use efficiency estimation algorithm using in situ hyperspectral and eddy covariance measurements for a maize canopy in Northeast China. Ecol. Evol. 7, 4735–4744.
- Zhang, Q., Chen, J.M., Ju, W., Zhang, Y., Li, Z., He, L., Pacheco-Labrador, J., Li, J., Qiu, B., Zhang, X., Qiu, F., Chen, B., Chou, S., Zhang, Z., Shan, N., 2021. Ground-based multiangle solar-induced chlorophyll fluorescence observation and angular normalization for assessing crop productivity. J. Geophys. Res. Biogeosci. 126 https://doi.org/10.1029/2020JG006082.
- Zhang, Yao, Xiao, X., Zhang, Yongguang, Wolf, S., Zhou, S., Joiner, J., Guanter, L., Verma, M., Sun, Y., Yang, X., Paul-Limoges, E., Gough, C.M., Wohlfahrt, G., Gioli, B., van der Tol, C., Yann, N., Lund, M., de Grandcourt, A., 2018. On the relationship between sub-daily instantaneous and daily total gross primary production: implications for interpreting satellite-based SIF retrievals. Remote Sens. Environ. 205. 276–289.
- Zhu, Y., Weindorf, D.C., Chakraborty, S., Haggard, B., Johnson, S., Bakr, N., 2010. Characterizing surface soil water with field portable diffuse reflectance spectroscopy. J. Hydrol. 391, 133–140.